

# Unraveling the Evolution of an Unusually Active Earthquake Sequence Near Sheldon, Nevada

D. T. Trugman \*<sup>1</sup>, W. H. Savran <sup>1</sup>, C. J. Ruhl <sup>1,2</sup>, K. D. Smith <sup>1</sup>

<sup>1</sup>Nevada Seismological Laboratory, University of Nevada, Reno, Reno NV, USA, <sup>2</sup>Verisk, Boston MA, USA

**Author contributions:** *Conceptualization:* D. Trugman, K. Smith, C. Ruhl. *Data Curation:* D. Trugman. *Formal Analysis:* D. Trugman, W. Savran. *Funding Acquisition:* D. Trugman, K. Smith, W. Savran. *Investigation:* D. Trugman, W. Savran, K. Smith, C. Ruhl. *Methodology:* D. Trugman, W. Savran. *Project Administration:* D. Trugman. *Resources:* D. Trugman, W. Savran. *Software:* D. Trugman, W. Savran. *Supervision:* D. Trugman. *Validation:* D. Trugman, W. Savran. *Visualization:* D. Trugman, W. Savran. *Writing – original draft:* D. Trugman, K. Smith. *Writing – review & editing:* D. Trugman, W. Savran, K. Smith, C. Ruhl.

**Abstract** One of most universal statistical properties of earthquakes is the tendency to cluster in space and time. Yet while clustering is pervasive, individual earthquake sequences can vary markedly in duration, spatial extent, and time evolution. In July 2014, a prolific earthquake sequence initiated within the Sheldon Wildlife Refuge in northwest Nevada, USA. The sequence produced 26 M<sub>4</sub> earthquakes and several hundred M<sub>3</sub>s from 2014 through 2018, with no clear mainshock or obvious driving force. Here we combine a suite of seismological analysis techniques to better characterize this unusual earthquake sequence. High-precision relocations reveal a clear, east-dipping normal fault as the dominant structure that intersects with a secondary, subvertical cross fault. Seismicity occurs in bursts of activity along these two structures before migrating down-dip and eventually transitioning to shallower structures to the east. Inversion of nearly one hundred moment tensors constrain the overall normal faulting stress regime. Source spectral analysis suggests that the stress drops and rupture properties of these events are typical for tectonic earthquakes in the western US. While station coverage is sparse in this remote study region, the timely installation of a temporary seismometer allows us to detect nearly 70,000 earthquakes over a 40-month time period when the seismic activity is highest. Such immense productivity is difficult to reconcile with current understanding of crustal deformation in the region and may be facilitated by local hydrothermal processes and earthquake triggering at the transitional intersection of subparallel fault systems.

**Non-technical summary** It is sometimes said that earthquakes hunt in packs, and there is perhaps no clearer example of this phenomena than a recent earthquake sequence within the Sheldon Wildlife Refuge in the northwest corner of Nevada, USA. Over a three-year time period, we detected more than 70,000 earthquakes occurring over a spatial footprint of ~5km x 5km. This article uses advanced seismological techniques to examine the Sheldon sequence in great detail to better understand the factors driving it. Earthquakes are a regular facet of life in western Nevada and California, so an improved understanding of seismicity and earthquake processes can help mitigate risks posed to communities near active fault systems.

## 1 Introduction

A remarkable sequence of earthquakes occurred in the far northwest corner of Nevada within the Sheldon National Wildlife Refuge. The sequence began in July of 2014 and featured high seismicity rates through 2016, producing 262 earthquakes with local magnitude  $M_L$  3 and greater, and 26 larger than  $M_L$  4, with the largest event of  $M_L$  4.73 (November 9, 2015, 13:55 UTC). Of these, ~100 well-constrained moment tensors were generated by the Nevada Seismological Laboratory (NSL), with the vast majority of solutions showing normal faulting in a WNW directed extension direction (T-axis) with a small oblique component. The spatiotemporal evolution of the sequence is complex, featuring several distinct periods of activity, each including several M<sub>4</sub> events with no clear mainshock throughout. The objective of this article is to provide a comprehensive analy-

sis of the Sheldon sequence informed by a diverse array of seismological techniques, including high-precision earthquake locations, detection of small earthquakes using machine learning algorithms, moment tensor inversions, and source spectral analysis. As we will demonstrate, the Sheldon sequence has unique characteristics but is representative of a broader pattern of highly productive earthquake sequences throughout the Walker Lane in recent years (Hatch-Ibarra et al., 2022; Ross et al., 2019; Ruhl et al., 2016a,b, 2021; Trugman et al., 2023; Trugman and Shearer, 2017b).

Earthquake locations for events early in the sequence are poor due to the sparse seismic station coverage in a remote region of northwest Nevada. Stations from partner networks in California (NC and BK), Oregon (UO), and Washington (UW) were incorporated into routine NSL processing and provided key coverage throughout the Sheldon sequence (Figure 1). Overall, 7966 earthquakes could be located. As activity rates and event

Production Editor:  
Carmine Galasso  
Handling Editor:  
Andrea Llenos  
Copy & Layout Editor:  
Oliver Lamb

Received:  
June 20, 2023  
Accepted:  
August 15, 2023  
Published:  
September 26, 2023

\*Corresponding author: dtrugman@unr.edu

magnitudes increased, by November 18, 2014, the NSL had installed a 6-channel (broadband and strong motion) portable station, COLR, on private land at a distance of approximately 16 km from the central part of the sequence and with reliable cellular communications to Adel, Oregon (about 30 km to the northwest). Access to the Sheldon National Wildlife Reserve wilderness study area was restricted. Temporary station COLR provided high signal quality for body wave phase identification critical to developing high-precision event locations and machine learning detections for the remainder of the sequence. The site operated through February 6, 2018, contributing more than three years of continuous recordings.

Geologically, the Sheldon sequence occurred directly east of a series of 16.5 and 15.5 Ma, mid-Miocene silicic centers, the High Rock Caldera Complex (HRCC), and associated flood basalts (Coble and Mahood, 2016). These volcanics, along with McDermitt Caldera complex to the east, have been considered the initiation of the NE trending Snake River Plain-Yellowstone hot-spot system (Henry et al., 2017; Pierce and Morgan, 1992). Flood basalts aged 15 Ma and younger east of the HRCC (Coble and Mahood, 2016) cover the source area of the Sheldon sequence. Faulting within the basaltic tablelands is most likely much older and definitive extensive Quaternary faulting has not been identified.

Current Basin and Range extensional faulting is concentrated along the eastern Warner Range in Surprise Valley about 50 km west of the Sheldon sequence (Lerch et al., 2010, Figure 1). Slip rates for the Surprise Valley fault have been estimated to be 1 mm/yr and larger. Potential geothermal resources in Surprise Valley have resulted in several studies. The paleoseismic transect of northwest Nevada presented by Personius et al. (2017) did not establish significant post-15Ka extensional faulting comparable to Surprise Valley deformation near the Sheldon source area. It did, however, speculate on minor potential structures within Long Valley, a basin in northwest Nevada that borders Miocene tablelands and escarpments adjacent to the Sheldon sequence (Figure 1). There is nothing in the post Miocene geology that may represent deformation events associated with Sheldon sequence. However, the Long Valley feature within the basaltic volcanic terrain extends for approximately 150 km north-south and includes the 1968 Adel, Oregon earthquake sequence (described below).

The most notable recent earthquake activity in the vicinity of the Sheldon sequence in occurred at Adel, in southeast Oregon in 1968 (Schaff, 1976, Figure 1). The largest earthquake of the 1968 sequence was an  $M_L$  5.1 on May 30 and caused structural damage in the community of Adel. The nascent NSL at the time deployed a local telemetered 4-station analog portable seismic array and was able to constrain a north striking left-lateral oblique short period focal mechanism for the mainshock with as many as 200 events recorded per day during the aftershock sequence. Nearly fifty years later, an equally notable sequence occurred less than 40 km to the southeast in the Sheldon Wildlife Refuge. This article is a report on what unfolded.

## 2 Data and Methods

In the following sections, we overview the data acquisition, processing, and analysis steps we used to characterize the Sheldon sequence. Derived datasets produced as part of this study, along with the velocity model used in the location analysis, are archived on Zenodo (see Data and code availability section).

### 2.1 Catalog and Waveform Data

For the purpose of earthquake monitoring in the state of Nevada, the NSL maintains an Antelope Datascope database of phase arrivals, associated events, and continuous waveforms from regional stations operated by the NSL and partner networks. All phase arrivals (at public stations) and earthquake origins determined by the NSL are also submitted to the US Geological Survey Comprehensive Catalog (ComCat) for public dissemination. For each reviewed and cataloged event in the Sheldon study region (Figure 1), we extract P and S arrival times from the database, as well as segments of waveform data (and metadata) encompassing these phases, from all recording stations within 250 km. Station coverage is generally sparse in this region, rendering focal mechanism determination through first motion polarity analysis unviable. Station COLR is the closest (~16 km) broadband sensor by a considerable distance (BK station MOD is ~56 km), so we also compile continuous data waveform from this station for its entire operating period (November 2014 to February 2018) for the purposes of small earthquake single-station detections. Moment tensor inversions may benefit from recordings at greater distances than are archived routinely by the NSL, and thus the waveform data and metadata used for that purpose is downloaded as a separate process (Beyreuther et al., 2010; Owens et al., 2004).

### 2.2 Earthquake Locations

We begin our analysis by working to refine the earthquake locations of reviewed events in the NSL database. Our two-step procedure involves both absolute location estimates based on analyst phase arrival picks and relative relocation refinements informed by waveform cross-correlation. In the first step, we estimate absolute locations by applying the NonLinLoc algorithm (Lomax et al., 2000, 2001) to the NSL phase arrival bulletin and a 1D velocity model. The NonLinLoc algorithm explicitly accounts for station elevations when computing travel time grids, but there can still be systematic station-specific misfits due to unmodeled subsurface velocity structure. To account for this, we first do an initial run of NonLinLoc to estimate the correction term for each station-phase combination, and then rerun the location algorithm after applying the correction term to the arrival time data to achieve the final solution.

We next refine the absolute locations obtained by NonLinLoc using GrowClust3D.jl (Trugman et al., 2022), a relative relocation technique that leverages precise differential travel times measured from waveform cross-correlation of pairs of events recorded at common stations. For these measurements, we focus on

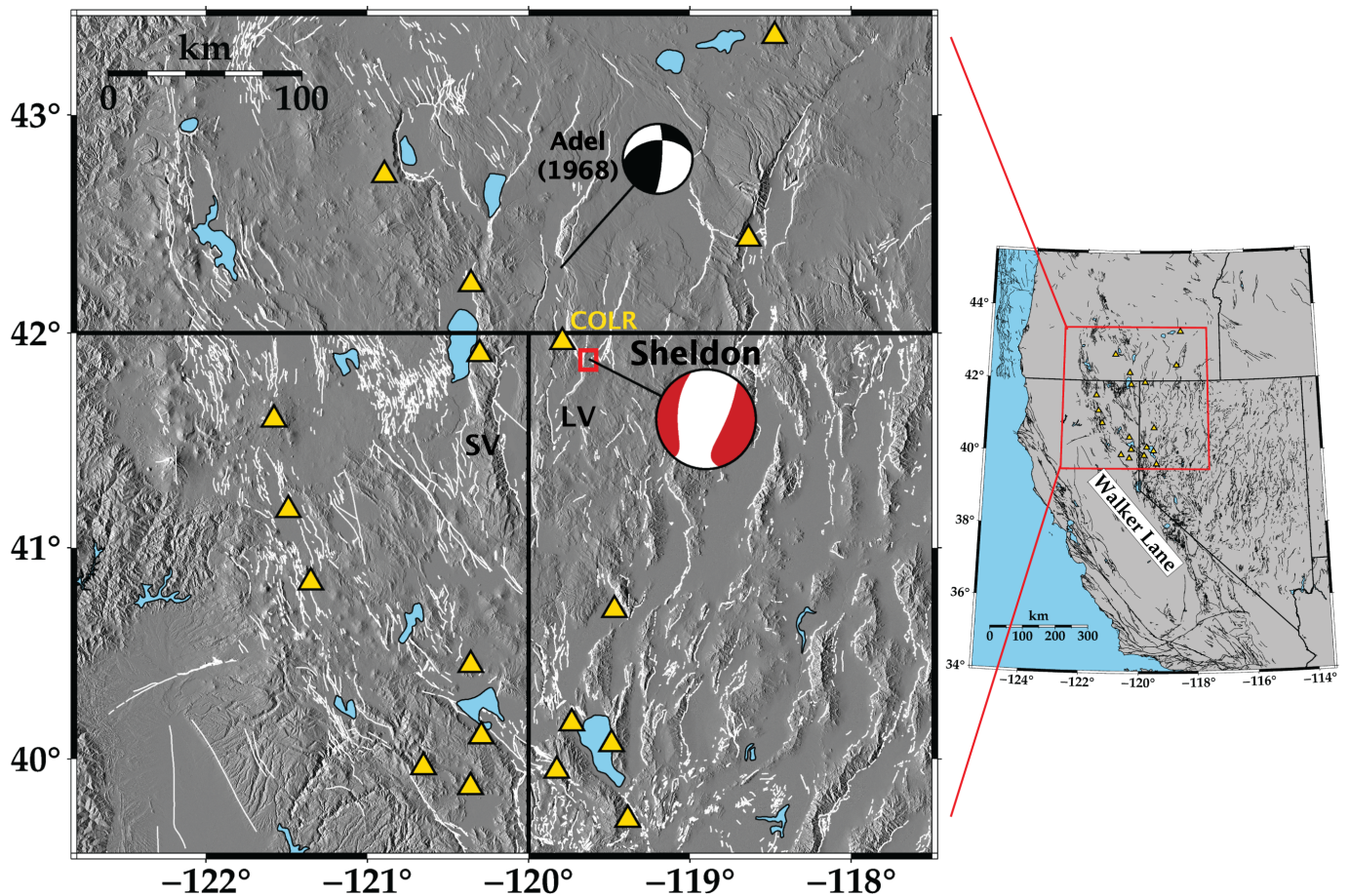


**Figure 1** Overview map of the study region and its position within the western US (inset). Earthquakes concentrate within the Sheldon Wildlife Refuge, marked in red. Regional stations used in location analysis are marked as gold triangles. A normalized *Kostrov* (1974) summation of Sheldon moment tensors (red mechanism) demonstrates that normal faulting predominates during the sequence. The location of the 1968 Adel earthquake sequence, as well as the Surprise Valley (SV) and Long Valley (LV) fault zones are marked for reference.

a subset of events with  $M_L$  1.0 and greater. We identify all pairs of nearby events within 5 km distance, and cross-correlate separately both P and S waveform windows at all stations recording both events. We band-pass filter the waveforms from 1-12 Hz and measure P and S differential times using 1.5 s and 2.5 s windows, respectively (Trugman et al., 2020); start times for time windows are determined at stations without listed phase arrivals through use of theoretical arrival times, which are later refined by cross-correlation (Trugman and Shearer, 2017a). Differential travel times are measured from the peaks of each cross-correlation function by applying a spline interpolation approach with subsample precision; measurements are discarded if the peak sidelobe is within 0.10 units of absolute amplitude of the peak value. The differential travel time database is then used as input to the GrowClust3D.jl software package, which uses a clustering algorithm to perform relative event relocations using the same station-specific travel time grids generated by NonLin-Loc. For quality-control purposes, we use only differential times with cross-correlation value of 0.65 or greater and require at least 8 qualifying differential times to retain an event pair. With this workflow and quality control, we relocate 3811 of 6533 events with  $M_L$  1.0 and greater. We use the events with refined positions as the

basis for the structural interpretation of the sequence.

### 2.3 Moment Tensor Inversions

Because sparse azimuthal station coverage precludes reliable focal mechanism estimates, moment tensor inversions provide the most robust means of obtaining information about the style of faulting for earthquakes in the Sheldon sequence. To this end, we use MTINV (Ichinose et al., 1998), a time-domain inversion algorithm applied to long-period surface waves recorded at regional distances. Three-component waveforms are downloaded from all available stations with HH and BH channels within a search radius that depends on the earthquake size (generally 300 – 500 km) from regional data centers. Moment tensor inversions of this form are generally feasible for earthquakes of mid-magnitude 3 and greater; smaller earthquakes do not produce sufficient long-period energy. Because of the extreme productivity of the Sheldon sequence, we are able to complete more than 100 such inversions, and use a quality-controlled subset of 93 moment tensor solutions with variance reduction >40% for our seismotectonic analysis.

## 2.4 Earthquake Detections at Station COLR

The earthquakes listed in NSL and ComCat event databases are those that are well-recorded enough at regional distances to produce a viable location estimate. Because relatively few stations are located within 100 km of the Sheldon sequence, this database only includes events that are large enough to be clearly seen at these distances. If we instead focus on the problem of detection rather than location, it is possible to compile a much more complete listing of events and their approximate size through detailed analysis of the COLR station, which is the closest to the source region and whose broadband sensor can record small earthquakes with high fidelity. In this way we recover a detailed time history of the sequence at very small magnitudes, significantly below the network detection threshold for this station distribution geometry. The key assumption here is that nearly all of the arrivals observed at COLR that are not seen at more distant stations (and hence missing from the analyst arrival database) are in fact coming from the Sheldon sequence and not from another source. This is plausible, given the low background seismicity and extreme event rates near Sheldon during this deployment, and can be confirmed if the detections exhibit short S-minus-P times indicative of a local source.

We apply the open-source SeisBench package (Woolam et al., 2022) to detect P and S arrivals on continuous, three-component waveforms at station COLR from November 2014 through February 2016. We use the EQ-Transformer model architecture (Mousavi et al., 2020) trained on the Stanford Earthquake Dataset (Mousavi et al., 2019), saving all arrivals with detection probabilities  $>0.1$ . We remove duplicate arrivals and those with unusually low signal-to-noise, and group the remaining arrivals into events using a simple temporal clustering algorithms (typical S minus P times at this distance are  $<3$  s and thus are simple to associate). For each detected event, we also measure the equivalent Wood-Anderson displacement  $A_{mm}$  (in millimeters) and use that to calculate a single-station local magnitude estimate consistent with the definition used for other NSL events:

$$M_L = \log_{10} A_{mm} + A_0(R) \quad (1)$$

where  $A_0(R)$  is a nonparametric distance-correction term (Richter, 1935). Each detected event thus comes with an origin time and magnitude estimate, assuming an approximate distance of 16 km from to station COLR. This is a reasonable approximation given the sequence's spatial footprint of  $\sim 5$  km  $\times$  5 km, over which the distance correction to the magnitude scale varies by about 0.1 magnitude unit.

## 2.5 Source Spectral Analysis

Earthquake source spectra can provide useful insight into the rupture characteristics of individual earthquakes. Source spectral measurements are often interpreted in relation to a theoretical model in which the low-frequency asymptote  $\Omega_0$  of the displacement source spectra is proportional to seismic moment, and the corner frequency  $f_c$  that marks the transition to high-frequency spectral decay is inversely proportional

to the characteristic source duration of the earthquake (Boatwright, 1980; Brune, 1970; Madariaga, 1976; Sato and Hirasawa, 1973). A key challenge in the analysis of source spectra is the need to correct for path and site effects to isolate the source contribution to the recorded spectrum (Abercrombie, 2021; Anderson and Hough, 1984; Hanks, 1982; Hough, 1996). This problem is particularly acute for the Sheldon sequence, where most of the stations used in the earthquake locations are at distances greater than 100 km, where the spectrum at moderate and high frequencies is severely attenuated.

Station COLR is a notable exception, with high-quality recordings of thousands of moderate and large events at a distance less than 20 km. There have been few normal faulting Walker Lane sequences, and none with this range of magnitudes, to begin to assess regional normal faulting source processes. For these reasons, we focus our analysis on the spectra recorded at COLR. Such single-station measurements should be treated with appropriate caution, as they inevitably neglect variations in spectral amplitude across the focal sphere that are caused by radiation pattern and directivity effects. Despite this concern, any assessment of the source spectral properties of these earthquakes has the potential to provide useful insight into the rupture characteristics of these earthquakes that complements well the other techniques used in this study.

The S-wave spectra of earthquakes recorded on the broadband seismometer at COLR generally exhibit good signal-to-noise (SNR) ratios for earthquakes of  $M_L$  2.0 and greater within the 0.5-20.0 Hz frequency band. For each such earthquake, we estimate S-wave spectra from the vector summation of both horizontal components using the multitaper technique of Prieto et al. (2009). Time windows for the spectral estimates are magnitude-dependent and increase from 6.0 s at  $M_L$  2.0 to 16.0 s at  $M_L$  4.5. Note that these relatively long time windows may include some of the S-wave coda, which could suppress directivity effects (which we neglect in this work). Spectra are converted in the frequency domain into units of displacement and resampled with 75 logarithmically spaced data points from the 0.2 – 20 Hz. We exclude from analysis individual frequencies points with SNR  $<3$  and discard all spectra in which 20% or greater of frequency points qualify as low SNR by this criterion.

We perform two types of analyses on this dataset of COLR spectra. First, for each event (regardless of size) we measure the spectral moment  $\Omega_0$  from the low-frequency asymptote and use this to estimate the seismic moment  $M_c$  of the earthquake, after correcting for distance ( $R$ ), radiation pattern ( $U_{\phi\phi}$ ), and surface amplification effects ( $F$ ):

$$M_0 = \frac{4\pi\rho c^3 R\Omega_0}{FU_{\phi\phi}} \quad (2)$$

where  $\rho$  and  $c$  are the density and wavespeed (e.g., Aki and Richards, 2002).

This allows us to calibrate an  $M_L$  -  $M_W$  relation for this dataset that is useful in quantifying the total moment release of the sequence. Second, for a subset of 42 large events ( $M_L$  3.5 and greater recorded by COLR),

we identify nearby smaller events ( $M_L$  2-3) as empirical Green's functions (EGFs) and form spectral ratios with the EGFs to correct for path and site effects (e.g., Hough, 1997). Candidate EGFs in this magnitude range are selected based on their spatial proximity (<3 km distance laterally and vertically) and cross-correlation with the larger target event. Here we select EGFs with correlation values greater than 0.75 in a frequency band 0.5 - 1.25 Hz, which is above the low-frequency noise band at COLR and below the corner frequency of  $\sim M_L$  3.5 target events (Abercrombie, 2015; Abercrombie et al., 2017; Ruhl et al., 2017); we would not expect even high-quality EGFs to correlate with the targets above their corner frequency.

We input each such spectral ratio associated with a target event into a Bayesian inference algorithm in which the primary objective is to measure the target event corner frequency and its uncertainty (Trugman, 2022). For this work, we assume a Brune (1970) spectral model of the form:

$$S_i(f) = \frac{\Omega_0}{1 + (f/f_c)^2} \quad (3)$$

each event (EGF and target), which yields a spectral ratio model of the form:

$$R_{ij}(f) = \frac{\Omega_{0[i]} 1 + (f/f_{c[j]})^2}{\Omega_{0[j]} 1 + (f/f_{c[i]})^2} \quad (4)$$

where the indices  $i$  and  $j$  denote target and EGF events respectively.

Bayesian inference is implemented through the PyMC software package (Salvatier et al., 2016), which uses the No U-Turns formulation of the Hamiltonian Monte Carlo algorithm (Hoffman and Gelman, 2011) to draw samples from the posterior distribution. The likelihood function that connects model parameters to observations is  $T$ -distributed, which helps to account for outlier data points common in spectral ratios (Trugman, 2022). Prior distributions for the moment ratio and target and EGF corner frequencies are weakly informative and magnitude-dependent (Trugman, 2022), scaling self-similarly with a median stress drop of 5.0 MPa. The results are not sensitive to the detailed parameterizations of the prior distributions, since each target event inversion is constrained by tens to hundreds of EGFs, and thus the data carries the dominant weight in the posterior parameter estimates (Trugman, 2022). We focus our analysis on the corner frequencies of the target events and not the EGFs, since the latter have large uncertainties as they are each constrained by a single spectral ratio. One advantage of this Bayesian framework is the inherent stability of the prior distributions imposed on EGF source parameters, which work to mitigate the potential for biasing mainshock source parameter estimates when EGF parameters are poorly constrained from lack of data (Shearer et al., 2019).

## 3 Results

### 3.1 Earthquake Locations and Sequence Time Evolution

As may be anticipated by the sparse station coverage, the initial absolute locations from NonLinLoc are highly scattered and uncertain, without any discernable structure (Figure 2a). These results are comparable to the locations from the ComCat database, which use the same phase arrival inputs but a slightly different velocity model suitable for statewide monitoring purposes. After applying GrowClust3D.jl however, the picture sharpens dramatically (Figure 2b). In map view, there is a dominant structure trending NNE and dipping to the east, and a secondary branch arcing NNW. These structures are presently unmapped, positioned several kilometers to the east of the Warner Valley fault, a west-dipping system listed in the USGS Quaternary Faults and Folds Database (USGS and CGS, 2006). The secondary NNW branch aligns particularly well with visible features of the surface topography. There is also another shallower cluster of seismicity to the east, closer to the mapped Guano Valley fault system.

The geometry of sequence is best seen in cross section (Figure 2c) or visualized in 3D (Movie S1). Here the eastward dip of the main fault is readily distinguished (dip angle  $\sim 67^\circ$ ), with the secondary NNW-trending cross structure at a steeper, subvertical angle. Earthquake locations for this sequence are best resolved from November 2014 through February 2018 when station COLR was operational, which captures the bulk of the sequence but misses the initial few months.

The spatiotemporal evolution during this time period is quite complex and again is best visualized in animated form (Movie S2). The seismicity exhibits no systematic migration or diffusion pattern, but instead features multiple waves of activity separated by times of near quiescence (Figure 3). The most notable such instance occurs in May 2015, where seismicity nearly shuts off before a second burst of events, including several  $M_W$  4 earthquakes, occurs in July 2015. During the first year of the sequence, most earthquakes occur on either the primary, east-dipping fault or the steeply dipping secondary NNW striking cross-fault. The shallow cluster of events to the east of these structures initiates later in the sequence, starting in December 2015. There is also a general tendency for events occurring later in the sequence to occur deeper on the main structures than in the early part of the sequence, perhaps indicating a down-dip migration. Following this overall evolution of the sequence, the primary structures' activity rates decline and the sequence is essentially over.

### 3.2 Moment Tensor and Source Spectral Analysis

With its plethora of moderate magnitude events, the Sheldon sequence is particularly amenable to moment tensor inversions, and we analyze 93 quality-controlled solutions as part of this study. We display the results in map view (Figure 4a), color-coding each mechanism by the mean horizontal strain  $\epsilon_M$  implied by the

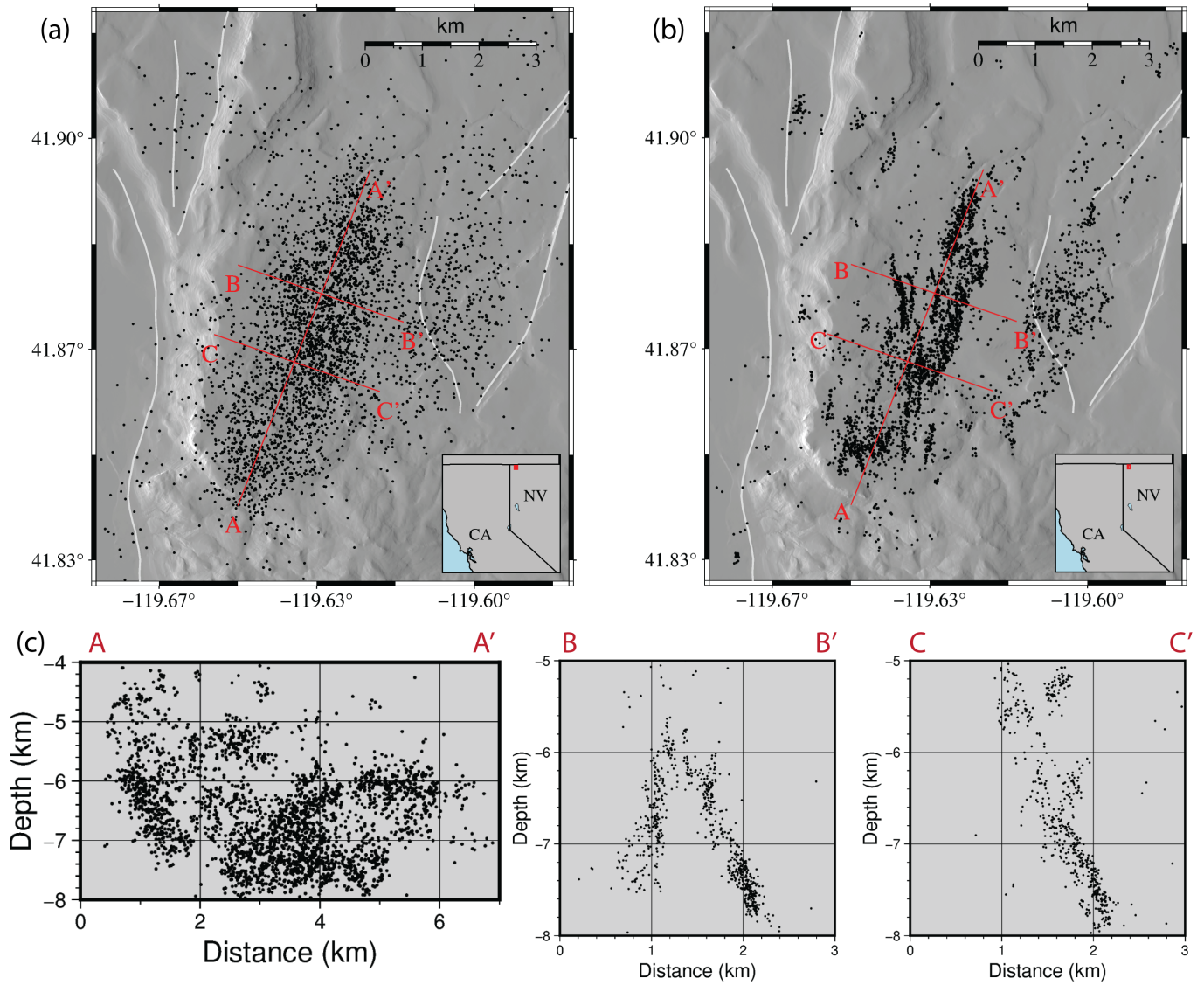


**Figure 2** Relocation of the Sheldon sequence. (a) Initial epicentral locations in map view output by NonLinLoc, with faults from the USGS Quaternary faults database marked in white. (b) Refined locations of these events after applying Grow-Clust3D.jl. (c) Cross-sections of relocated seismicity, with AA', BB', and CC' defined in panel (b).

moment tensor components in geographic coordinates (e.g. Becker et al., 2018):

$$\epsilon_M = \frac{\epsilon_{EE} + \epsilon_{NN}}{2} \quad (5)$$

Here negative values indicate horizontal compression (thrust faulting), while positive values indicate extension (normal faulting). Most are normal faulting events, though several that align with the secondary cross-structure are strike-slip. The spatial density of high-quality moment tensor measurements also allows us to constrain the regional stress orientation under the assumption that on average, slip vectors are aligned with the shear direction resolved on individual fault planes (Angelier et al., 1982; Gephart and Forsyth, 1984; Michael, 1984, 1987). Here we adapt the iterative approach proposed by Vavryčuk (2014) that applies a Coulomb instability criterion to identify the active fault plane of each mechanism, which is a-priori ambiguous due to the symmetry of the seismic radiation pattern. We do not seek to resolve spatial or temporal variations in the stress field (Hardebeck and Michael, 2006), just its

average value and uncertainty in our study region. We estimate the orientations of the three principal stresses ( $S_1$ ,  $S_2$ , and  $S_3$ ) and the shape ratio of principal stress magnitudes:

$$R = \frac{S_1 - S_2}{S_1 - S_3} \quad (6)$$

that best fits our dataset, with uncertainties obtained from bootstrap resampling. As expected, the stress orientations are consistent with an extensional regime (Personius et al., 2017) with a modest oblique component (Figure 4b):  $S_1$  is subvertical (plunge of 71°) with azimuth of 18°, while  $S_2$  is subhorizontal (plunge of 19°) with an azimuth of 194°.

Through our spectral ratio analysis, we obtain corner frequency measurements for 42  $M_L \geq 3.5$  and greater target events recorded by COLR (Figure 5). The primary outcome of this analysis are measurements of corner frequency which we can then translate to a stress drop value under the assumption of a circular source:

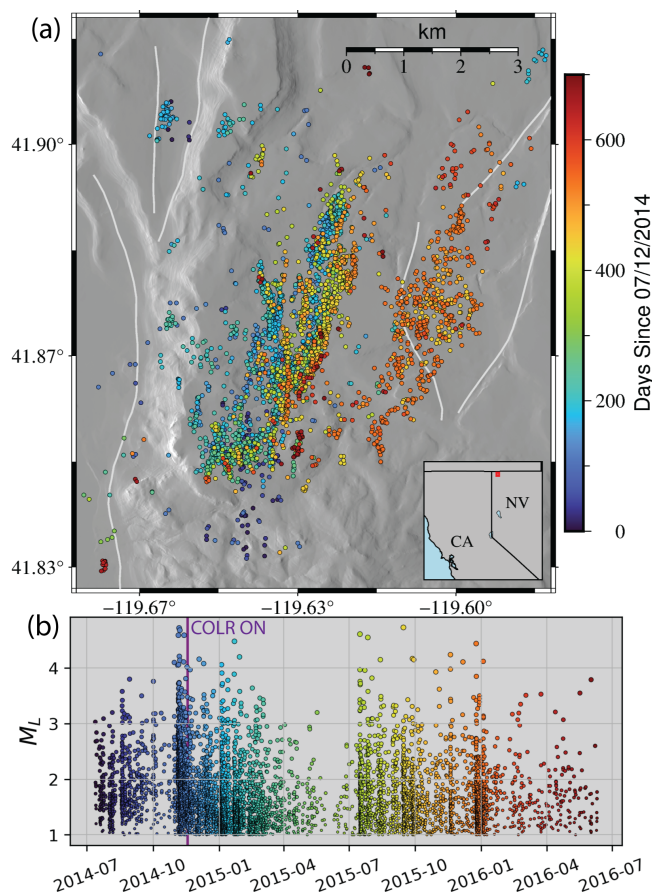


**Figure 3** Time evolution of the Sheldon sequence during the most active period (2014–2016). (a) Relocated seismicity in map view, color-coded by occurrence time. (b) Local magnitude  $M_L$  versus time, with colorscale consistent to (a). The start date of COLR recordings is marked for reference.

$$\Delta\sigma = \frac{7}{16} M_0 \left( \frac{f_c}{k\beta} \right)^3 \quad (7)$$

In this relation,  $\beta$  is the shear wavespeed at the source (a value we obtain from the velocity model) and  $k$  is a numerical constant that depends on the spectral model; here we use 0.26, appropriate for S-wave spectra with rupture velocities of 0.8–0.9  $\beta$  (Kaneko and Shearer, 2014). The distribution of stress drop values ( $\sim 0.5$ –20 MPa) obtained from this analysis is typical for tectonic earthquakes in California and Nevada (Abercrombie, 2013; Hatch et al., 2018; Ruhl et al., 2017; Shearer et al., 2022; Trugman, 2022; Trugman et al., 2023; Trugman and Shearer, 2017a), suggesting there is nothing particularly unusual about the rupture properties of the Sheldon events. It is worth emphasizing again that these results should be treated with some caution as they are obtained from a single, albeit high-quality, station.

### 3.3 Event-detection and Frequency-Magnitude Statistics

The magnitudes reported by the NSL are local magnitudes  $M_L$  obtained from equivalent Wood-Anderson displacements and corrected for distance (Richter, 1935). These values provide a useful measure of earthquake size, especially for small events, but do not allow one to assess the total moment released by the sequence. Moment tensors are available for most (but not all) of the

larger events and none of the smaller events, so there is a need to be able to approximate  $M_W$  in a consistent manner. To do this, we examine the moment measurements obtained through the spectral analysis at station COLR. The values are tightly correlated with independent measurements obtained in the moment tensor inversions (Figure 6a) and thus provide some confidence in their application.

Through least-squares regression analysis, we find a consistent scaling of the form:

$$M_W = 1.16 + 0.67M_L \quad (8)$$

for smaller earthquakes ( $M_L < 3.5$ ), above which the scaling appears nearly unity (Figure 6b). This break in scaling is well understood in terms of a transition point of the corner frequency of the earthquake with respect to the dominant frequencies of a Wood-Anderson measurement (Hanks and Boore, 1984; Munafo et al., 2016; Uhrhammer et al., 1996). We can use this piecewise linear relation to estimate  $M_W$  for all events without moment tensors, and then compute the total moment released during the sequence. This equates to about  $M_W$  5.6, with the greatest contributions coming from the bursts of seismicity starting in November 2014 and July 2015 (Figure 6c).

While they do not contribute much to this overall moment budget, very small earthquakes ( $M_L < 1$ ) can be detected on station COLR. After quality-control, our ma-

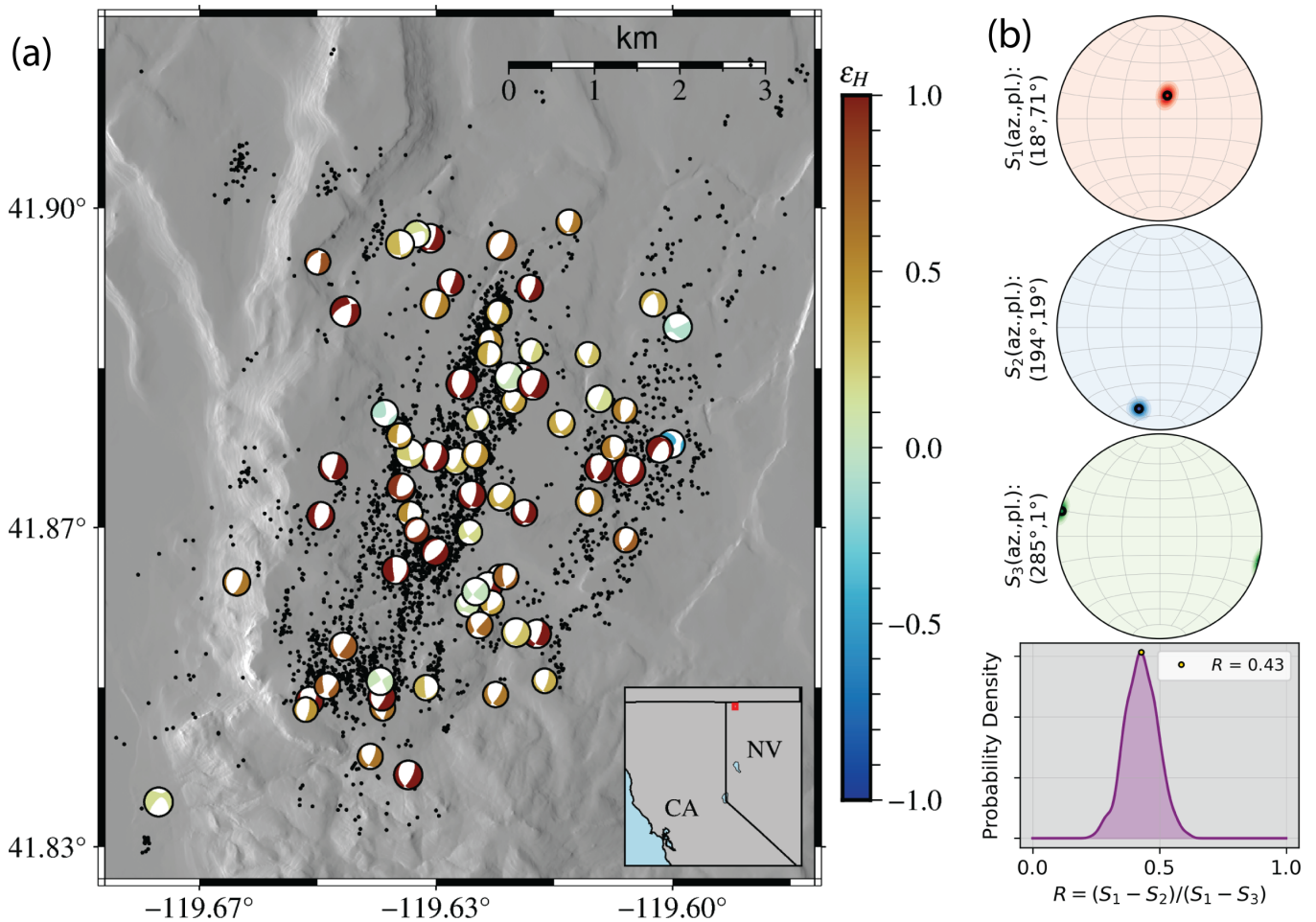


**Figure 4** Moment tensor and stress field analysis. (a) Moment tensors of relocated events, color-coded by normalized horizontal strain, where red colors indicate extension and blue colors indicate compression. (b) Results from stress inversion analysis, showing orientations of principal stresses  $S_1$ ,  $S_2$ , and  $S_3$ , as well as the shape ratio  $R$  defined in the text. Uncertainties come from 1000 bootstrap resamples of the input moment tensor dataset.

chine learning approach detects nearly 70,000 earthquakes during the time period in which the station is active, more than an order of magnitude greater than the number listed in the catalog during this time period. To confirm that these events are real and not false detections, we created a separate Antelope Datascope database to visualize the detected arrivals alongside existing analyst picks (Figure 7a). Manual scans of several active days confirm the quality of these detections, which identify nearly all of the analyst picks (Figure 7b; 97% have a machine learning arrival within 0.2s) along with more than 60,000 newly detected events. Short S-minus-P times for the detections confirm that these are local to the Sheldon area and not recordings of remote events. The time evolution of these detections (Figure 8a) is consistent with what is observed in the original monitoring catalog, including the bursts of seismicity interspersed with quiescent time periods noted above.

Through augmentation with our machine learning catalog, we are able to reduce the magnitude of completeness (for detected earthquakes) from 1.4 to 0.2 (Figure 7c). Using the “b-positive” estimator designed by van der Elst (2021) for robustness to potential changes in magnitude of completeness, we obtain a b-value for

the detection-augmented catalog of 0.74 (95% confidence interval of 0.730-0.754 via bootstrap resampling). This value is fairly typical for a tectonic earthquake sequence, if slightly on the low side, indicating a relative prevalence of large magnitude events compared to a sequence with a canonical b-value of 1.0 (Gutenberg and Richter, 1944). Note however that this b-value measurement corresponds to the local magnitude scale  $M_L$ . If we instead use equation (8) to convert the local magnitudes of small events to approximate moment magnitude, the b-value measurement would increase accordingly to  $\sim 1.1$ .

We also explore temporal variations in b-value by applying the b-positive estimator to sliding 1000-event windows (Figure 8), with uncertainties again obtained through bootstrap resampling. The initial part of the sequence captured by station COLR is characterized by relatively low b-values, with temporal fluctuations associated with bursts of seismicity. During the main part of the sequence (2014 – 2016), b-values remain mostly within the 0.65-0.85 range to within the uncertainties. From late onward, the b-value steadily increased to  $\sim 0.95$ , as large magnitude events became less frequent.

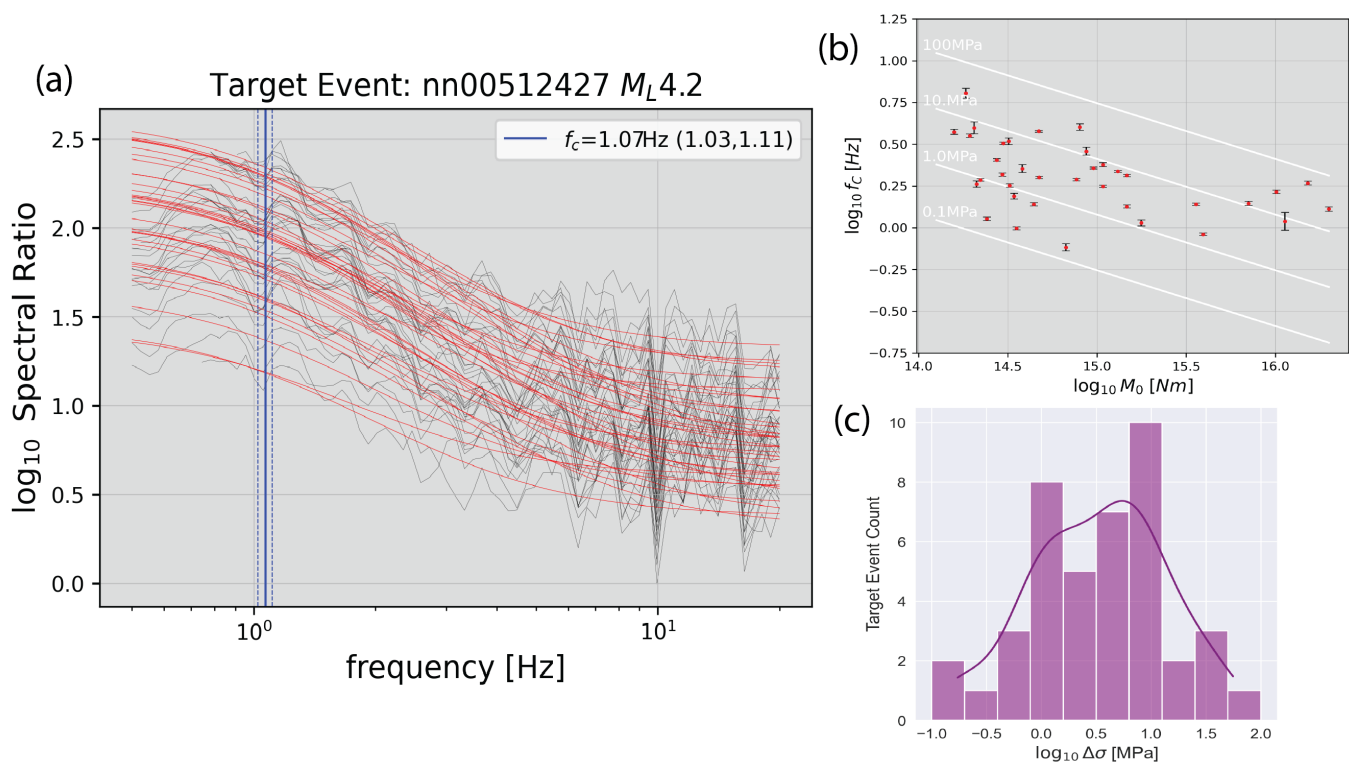


**Figure 5** Spectral ratio and stress drop analysis. (a) S-wave spectral ratios for an example  $M_L$  4.2 target event. Recorded spectral ratios with hundreds of EGFs are shown as black lines, and model fits are shown as red lines. The inferred target event corner frequency and uncertainty extracted from the posterior distribution are marked in blue. (b) Scaling of corner frequency with seismic moment for target earthquakes. (c) Distribution of target event stress drops.

## 4 Discussion

Our detailed analysis of the Sheldon earthquakes characterizes a highly productive sequence that initiated abruptly in the northwest corner of Nevada but does not provide any direct explanation for the physical forces that drive it. Seismicity in the Sheldon sequence is positioned at the intersection of the Warner Valley and Guano Valley fault systems listed in the Quaternary Faults and Folds Database (USGS and CGS, 2006), both of which have relatively low reported slip rates (<0.2 mm/yr). Most of the Sheldon earthquakes do not occur directly on either of these mapped faults, which dip mostly to the west and are geographically offset from the hypocentral positions. There likely exist other faults in between the Warner Valley and Guano Valley fault systems that are not in the USGS database that are either discernible in the local geomorphology or listed in older local geologic maps (Dohrenwend and Moring, 1991). Whether or not the Sheldon earthquakes lie on these liminal structures or ones that are completely invisible from their surface expression, the sequence is clearly positioned in the transitional zone of deformation between larger mapped systems.

The Sheldon sequence is by far the most prominent recent seismic activity in the northernmost Walker Lane (Figure 1), which is the tectonic province that marks the transition between strike-slip faulting in western California and extension in the Basin and Range (Busby, 2013; Faulds et al., 2005; Faulds and Henry, 2008; Hearn and Humphreys, 1998; Wesnousky, 2005). Sequences like Mogul (Anderson et al., 2009;

Bell et al., 2012; Ruhl et al., 2016a, 2017), Nine Mile Ranch (Hatch-Ibarra et al., 2022), Ridgecrest (Barnhart et al., 2020; Ross et al., 2019; Trugman et al., 2020), Lone Pine (Hauksson et al., 2020), Monte Cristo (Kariche, 2022; Ruhl et al., 2021; Sethanant et al., 2023; Zheng et al., 2020), and Antelope Valley (Pollitz et al., 2022; Trugman et al., 2023; Wang et al., 2023) exhibit high seismicity rates and aftershock productivity along complex and sometimes incipient fault structures, many of which were not well-mapped in advance of the sequence. Throughout most of the Walker Lane, transtensional crustal deformation is accommodated by an intricate tapestry of strike-slip and normal faults. The diversity of these sequences reflects this transtension, with some earthquakes occurring dominantly on strike-slip structures (e.g., Mogul, Nine Mile Ranch, Monte Cristo) and others dominantly on normal faulting structures (e.g., Lone Pine and Antelope Valley). Strike-slip faulting is the primary mode of deformation on northern Walker Lane faults (Chupik et al., 2021; Faulds et al., 2005; Gold et al., 2014; Koehler, 2019), but the Sheldon sequence is far enough north (past the Mendocino triple junction, for example) that it may well be classified as outside of the Walker Lane altogether. The dominant structure in this region along the northern California-Nevada border is the Surprise Valley fault (Figure 1), a classic Basin and Range normal faulting range front, striking north and accommodating down-to-the-east slip in an east-west extensional environment generally consistent with deformation in the Sheldon sequence. East of the Surprise Valley fault and south-

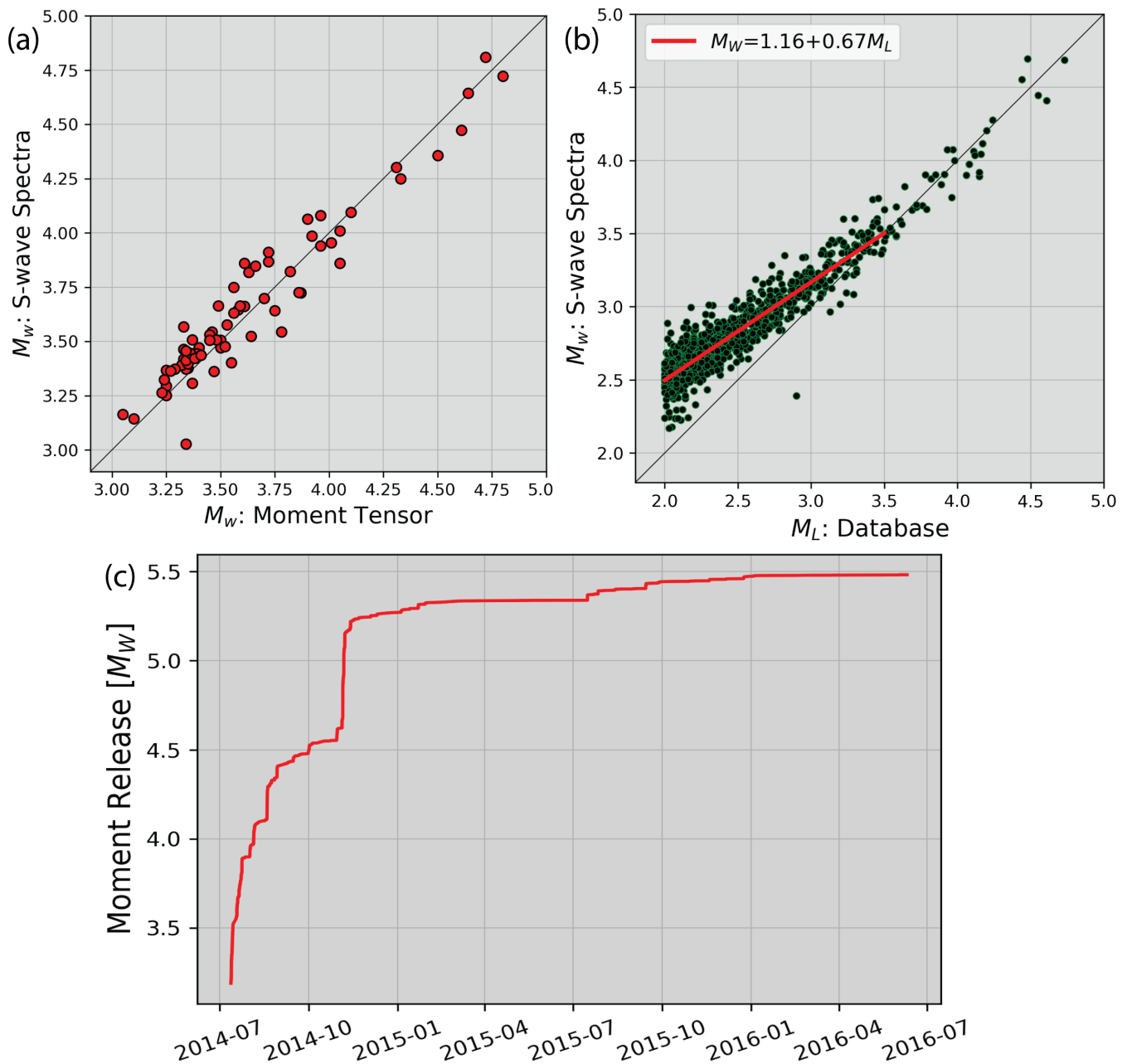


**Figure 6** Calibration of moment magnitudes. (a) Comparison of  $M_W$  estimates from moment tensors versus those obtained from S-wave spectra at station COLR. (b) Piecewise linear scaling relation of  $M_W$  and  $M_L$  obtained from S-waves at COLR. (c) Cumulative moment release versus time during the sequence.

west of the Sheldon sequence, the Long Valley fault system (Figure 1) has produced earthquakes as large as  $M7.0$  over the past 15 ka (Personius et al., 2017). The Sheldon sequence is subparallel to the complex network of faults confined within Long Valley and may fit within its broader deformation footprint.

The complex spatiotemporal evolution of the Sheldon sequence defies an easy description. Clearly, Sheldon is not a typical mainshock-aftershock sequence with a classic Omori (1894) decay in seismicity rate. The sequence is swarm-like in its persistent activity for several years duration (e.g., Hainzl, 2004; Hill, 1977; Mogi, 1963; Sykes, 1970), but its space-time progression shows no clear evidence of simple diffusion or migration patterns that could be readily linked to fluid injection or flow

(e.g., Ross et al., 2020; Shapiro et al., 1997) or aseismic slip (e.g., Sadeghi Chorsi et al., 2022; Koper et al., 2018; Lohman and McGuire, 2007) as the dominant driving force. No geodetic transients can be clearly observed in InSAR or regional permanent and campaign GPS measurements (Blewitt et al., 2018), which is perhaps unsurprising given the depth of seismicity and cumulative moment release equivalent to a mid  $M_W$  5 earthquake. The 2016-2019 Cahuilla swarm, another long-lived sequence in southern California (Cochran et al., 2023; Hauksson et al., 2019; Ross et al., 2020) provides a useful comparison to illustrate this point. While both sequences feature elevated seismicity rates over the course of several years, the Cahuilla swarm was characterized by a clear, radial migration pattern from a

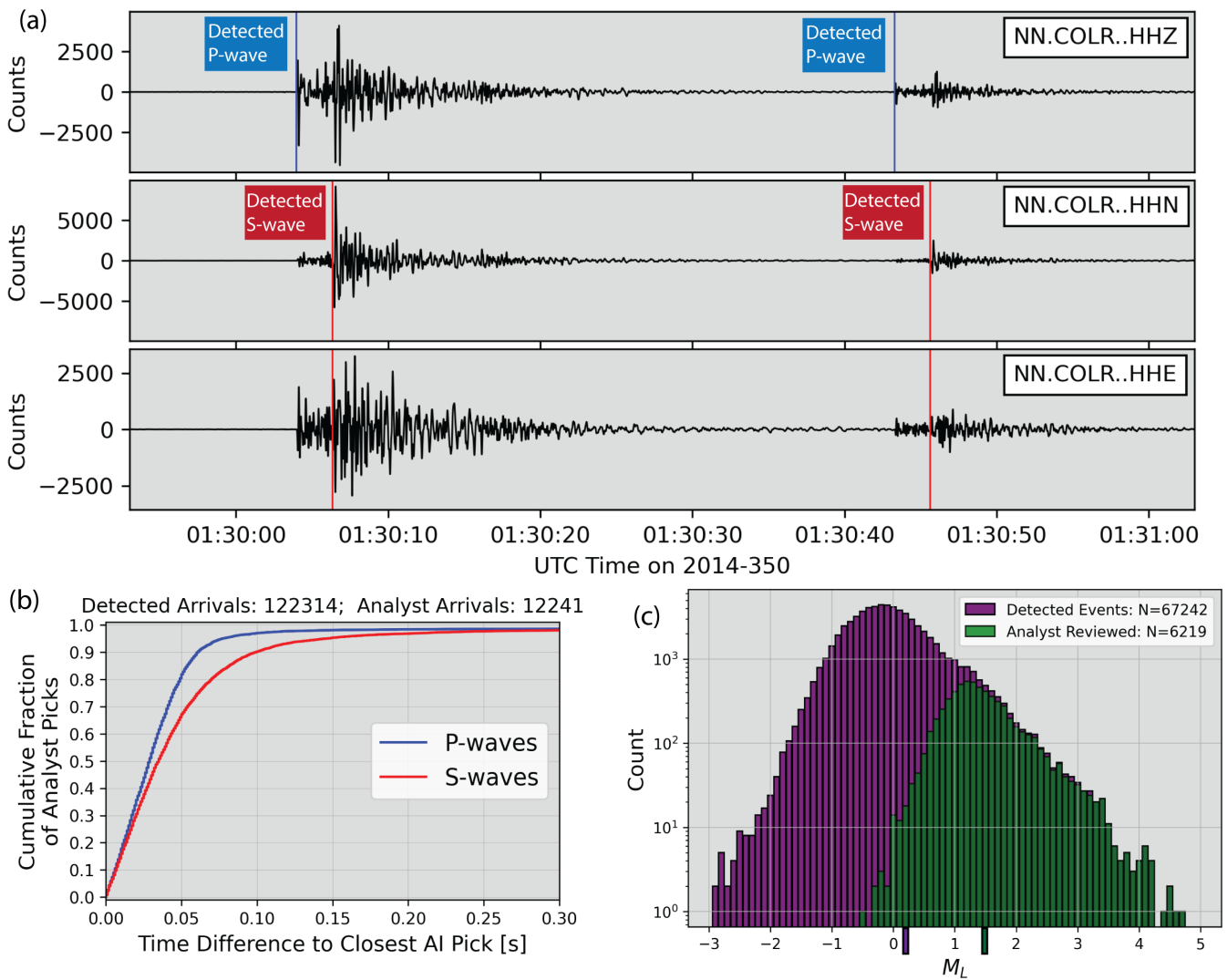


**Figure 7** Earthquake detections at COLR. (a) Examples of two small events detected by the machine learning algorithm from continuous data at COLR. The event shown on the left is a  $M_L$  2.0 event detected both by NSL analysts and the algorithm; their picks are overlapping (within 0.05s). The event shown on the right was too small for analysts to locate but was picked up by the algorithm. (b) Cumulative distribution of absolute time differences of analyst identified picks and the nearest machine learning pick. This figure shows, for example, that 95% and 90% of P-waves and S-waves (y-axis) have a machine learning phase arrival listed within 0.1s of the analyst pick (x-axis). (c) Comparison of magnitude distributions of detected events (purple) and cataloged events (green), with estimated magnitude of completeness for each catalog annotated on the x axis.

deep source point before triggering a  $M_L$  4 mainshock and subsequent seismicity (Ross et al., 2020). The Sheldon sequence, in contrast, did not exhibit such beautiful simplicity, with dozens of  $M_4$  events repeatedly triggered in a somewhat chaotic fashion.

The Sheldon sequence features several distinct waves of intense seismicity, each with several bursts of activity associated with one or more  $M_L$  4+ events, indicating the importance of earthquake triggering in sustaining, if not initiating, the sequence. In terms of spatial evolution, these phases include (i) an initiation of seismicity on the main NNE striking, E-dipping normal faulting structure, (ii) a subsequent illumination and complex migration patterns along an NNW trending, near-vertical cross fault, (iii) eventual migration down-dip to the east, and (iv) initiation of seismicity on shallower structures coincident with the Guano Valley faults. The overall productivity of the Sheldon sequence is truly

immense, featuring 26  $M_L$  4+ and 262  $M_L$  3+ events. For comparison, the 2008 Mogul, NV sequence (mainshock  $M_w$  4.9) produced two  $M_L$  4+ events and 38  $M_L$  3+ events in total. Although several studies have associated earthquake swarm activity with relatively high b-values (e.g., Holtkamp and Brudzinski, 2011; von Seggern et al., 2008), relatively low b-values we observe here (0.65 – 0.85) are consistent with other swarms in extensional tectonic settings within the shallow continental crust (Ruhl et al., 2016a; Ibs-von Seht et al., 2008). The gradual increase in b-value observed over time may indicate a relaxation in differential stress as the sequence progresses and eventually dissipates (e.g., Scholz, 1968, 2015). This trend is also reminiscent of the 2014 Long Valley Caldera swarm, where Shelly et al. (2016) interpret the b-value evolution in terms of a transition in fluid confinement, with earthquakes initially localized to select larger faults (lower b-value) before

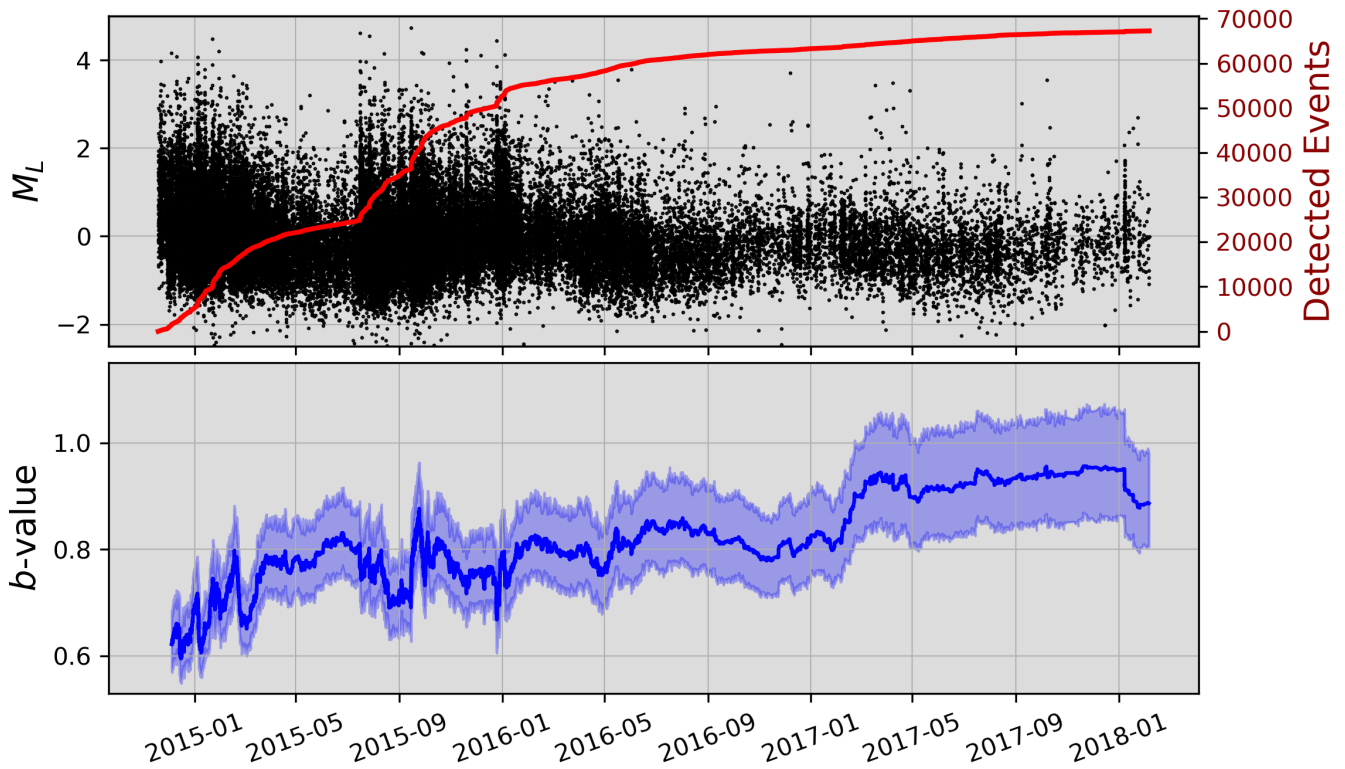


**Figure 8** Magnitude distribution and cumulative event count of machine-learning detection (top) and b-value time evolution (bottom); uncertainties are obtained from bootstrap resampling each 1000-event window used to compute the b-value at a given timestamp.

eventually diffusing outward in three dimensions and sampling additional, smaller faults (higher b-value). In the Sheldon sequence, the b-value is lower during the most active part of the sequence, where seismicity is confined to the two primary structures, and increases significantly in 2017 as these structures deactivate.

While there is no obvious signature of the driving force for the Sheldon sequence, its position in a transitional zone of deformation within a volcanic geologic context provides a viable explanation. Earthquake swarms are commonly associated with hydrothermal activity throughout the western United States (Chen and Shearer, 2011; Hauksson et al., 2013, 2019; Li et al., 2021; Lohman and McGuire, 2007; Mesimeri et al., 2021; Ross et al., 2020; Ross and Cochran, 2021; Shelly and Hardebeck, 2019; Vidale and Shearer, 2006) and globally (Cox, 2016; Hainzl, 2002, 2004; Ibs-von Seht et al., 2008), and often occur at the intersection of active faults or within otherwise transitional deformation zones (Hill, 1977; Sibson, 1987). The Sheldon sequence fits this paradigm well, positioned between the Warner and Guano Valley faults in a weak crustal zone associated with volcanic terrains. Seismic activity within the Sheldon sequence appears to be most intense at the intersection of the east-dipping normal fault and north-northwest-striking cross-fault, somewhat reminiscent of fracture mesh structures (Sibson, 1996) observed in several other studies of earthquake swarms and hydrothermal systems in the western US (Ross et al., 2017; Shelly et al., 2023). The complex patterns of seismicity we observe could perhaps be explained by the interaction of fluid movement

and earthquake-earthquake triggering, releasing elastic stresses built up progressively over time in this transitional deformation zone. While the remoteness of the Sheldon sequence makes it a challenging case study in providing the in-situ observations necessary to resolve the fine-scaled details of earthquake swarm dynamics, its occurrence is a useful reminder that such natural and violent swarm complexity can occur even in unexpected places in Nevada.

## 5 Conclusions

We characterize a highly active earthquake sequence beneath the Sheldon Wildlife Refuge in northwest Nevada using a broad set of seismological techniques. High-precision earthquake locations highlight a primary fault structure dipping to the east and a subvertical cross-fault striking north-northwest. Moment tensor and stress field analyses show results consistent with an overall normal faulting regime. The spatiotemporal progression of the sequence comprises repeated bursts of seismicity on these structures separated by quiescent periods. By leveraging machine learning algorithms, we detect nearly 70,000 events from 2014 – 2016. The physical factors driving the immense productivity of this sequence remain to be explained in full but are broadly consistent with models of earthquake swarms within transitional deformation zones and may combine both hydrothermal and earthquake triggering processes.

## Acknowledgements

D. Trugman gratefully acknowledges support from NSF Awards EAR-2231705 and EAR-2121666. NSL earthquake monitoring, data product, and field efforts were funded by the USGS Cooperative Agreement Number G20AC00038. We thank current and former NSL operations team members, including W. Honjas, D. Slater, A. Main, E. Wicks, R. Hatch-Ibarra, E. Morton, J. Borrman, T. Rennie, and G. Plank for their support and contributions to the earthquake monitoring and data products used in this study, as well as R. Abercrombie, C. Henry, and S. Wesnousky for helpful discussions on seismicity, geology and tectonics in Nevada. We also thank Associate Editor A. Llenos and two reviewers for their constructive comments that improved the manuscript.

## Data and code availability

We use phase arrival, event catalog, and waveform data products produced by the Nevada Seismological Laboratory (<http://www.seismo.unr.edu/Earthquake>) and publicly archived as part of USGS ComCat (<https://earthquake.usgs.gov/earthquakes/search/>) and delivered to the IRIS Data Management Center (<https://ds.iris.edu/ds/>). Quaternary faults and fold data were obtained from the USGS database (<https://www.sciencebase.gov/catalog/item/589097b1e4b072a7ac0cae23>), and surface topography downloaded from the USGS 3DEP program (<https://apps.nationalmap.gov/downloader/>). Waveform data were extracted using Antelope Software (<https://brtt.com>) and processed using ObsPy (Beyreuther et al., 2010). Additional analysis packages used, all publicly available, include NonLinLoc (Lomax et al., 2000, 2001), GrowClust3D.jl (Trugman et al., 2022), PyGMT (Wessel et al., 2019), and MTINV (Ichinose et al., 1998), mtspec (Krischer, 2016), and pymc (Salvatier et al., 2016). StressInversion.jl, a set of Julia software tools for stress inversions are publicly available on GitHub (<https://github.com/dttrugman/StressInversion.jl>). Regional waveforms for moment tensor inversion were downloaded using Standing Order for Data (Owens et al., 2004) and ObsPy (Beyreuther et al., 2010) programs. Supplementary Movies S1 and S2, along with the relocated catalog, velocity model, and moment tensor databases produced in this study are archived at Zenodo (<https://doi.org/10.5281/zenodo.8030954>). Full moment tensor solutions are also available on the Nevada Seismological Laboratory website (<http://www.seismo.unr.edu/Earthquake>).

## Competing interests

The authors have no competing interests to declare.

## References

- Abercrombie, R. Comparison of direct and coda wave stress drop measurements for the Wells, Nevada, earthquake sequence. *Journal of Geophysical Research: Solid Earth*, 118(4):1458–1470, 2013. doi: 10.1029/2012JB009638.
- Abercrombie, R. Investigating uncertainties in empirical Green's function analysis of earthquake source parameters. *Journal of Geophysical Research: Solid Earth*, 120(6):4263–4277, 2015. doi: 10.1002/2015JB011984.
- Abercrombie, R. Resolution and uncertainties in estimates of earthquake stress drop and energy release. *Philosophical Transactions of the Royal Society A: Mathematical, Physical and Engineering Sciences*, 379(2196):20200131, 2021. doi: 10.1098/rsta.2020.0131.
- Abercrombie, R., Bannister, S., Ristau, J., and Doser, D. Variability of earthquake stress drop in a subduction setting, the Hikurangi Margin, New Zealand. *Geophysical Journal International*, 208(1): 306–320, 2017. doi: 10.1093/gji/ggw393.
- Aki, K. and Richards, P. *Quantitative seismology*. University Science Books, Sausalito, Calif, 2nd edition, 2002.
- Anderson, J., Tibuleac, I., Anooshehpour, A., Biasi, G., Smith, K., and Seggern, D. Exceptional Ground Motions Recorded during the 26 April 2008 Mw 5.0 Earthquake in Mogul, Nevada. *Bulletin of the Seismological Society of America*, 99(6):3475–3486, 2009. doi: 10.1785/0120080352.
- Anderson, J. G. and Hough, S. A model for the shape of the fourier amplitude spectrum of acceleration at high frequencies. *Bulletin of the Seismological Society of America*, 74(5):1969–1993, 1984.
- Angelier, J., Tarantola, A., Valette, B., and Manoussis, S. Inversion of field data in fault tectonics to obtain the regional stress — I. Single phase fault populations: a new method of computing the stress tensor. *Geophysical Journal International*, 69(3):607–621, 1982. doi: 10.1111/j.1365-246X.1982.tb02766.x.
- Barnhart, W., Gold, R., and Hollingsworth, J. Localized fault-zone dilatancy and surface inelasticity of the 2019 Ridgecrest earthquakes. *Nature Geoscience*, 1–6, 2020. doi: 10.1038/s41561-020-0628-8.
- Becker, T., Hashima, A., Freed, A., and Sato, H. Stress change before and after the 2011 M9 Tohoku-oki earthquake. *Earth and Planetary Science Letters*, 504:174–184, 2018. doi: 10.1016/j.epsl.2018.09.035.
- Bell, J., Amelung, F., and Henry, C. InSAR analysis of the 2008 Reno-Mogul earthquake swarm: Evidence for westward migration of Walker Lane style dextral faulting. *Geophysical Research Letters*, 39(18), 2012. doi: 10.1029/2012GL052795.
- Beyreuther, M., Barsch, R., Krischer, L., Megies, T., Behr, Y., and Wassermann, J. ObsPy: A Python Toolbox for Seismology. *Seismological Research Letters*, 81(3):530–533, 2010. doi: 10.1785/gssrl.81.3.530.
- Blewitt, G., Hammond, W., and Kreemer, C. Harnessing the GPS Data Explosion for Interdisciplinary Science. *Eos*, 99, 2018. doi: 10.1029/2018EO104623.
- Boatwright, J. A spectral theory for circular seismic sources; simple estimates of source dimension, dynamic stress drop, and radiated seismic energy. *Bulletin of the Seismological Society of America*, 70(1):1–27, 1980.
- Brune, J. Tectonic stress and the spectra of seismic shear waves from earthquakes. *Journal of Geophysical Research*, 75(26): 4997–5009, 1970. doi: 10.1029/JB075i026p04997.
- Busby, C. Birth of a plate boundary at ca. 12 Ma in the Ancestral Cascades arc, Walker Lane belt of California and Nevada. *Geosphere*, 9(5):1147–1160, 2013. doi: 10.1130/GES00928.1.
- Chen, X. and Shearer, P. Comprehensive analysis of earthquake source spectra and swarms in the Salton Trough, California. *Journal of Geophysical Research*, 116(B9), 2011. doi: 10.1029/2011JB008263.
- Chupik, C., Koehler, R., and Keen-Zebert, A. Complex Holocene

- Fault Ruptures on the Warm Springs Valley Fault in the Northern Walker Lane, Nevada–Northern California. *Bulletin of the Seismological Society of America*, 112(1):575–596, 2021. doi: 10.1785/0120200271.
- Coble, M. and Mahood, G. Geology of the High Rock caldera complex, northwest Nevada, and implications for intense rhyolitic volcanism associated with flood basalt magmatism and the initiation of the Snake River Plain–Yellowstone trend. *Geosphere*, 12(1):58–113, 2016. doi: 10.1130/GES01162.1.
- Cochran, E., Page, M., Elst, N., Ross, Z., and Trugman, D. Fault Roughness at Seismogenic Depths and Links to Earthquake Behavior. *The Seismic Record*, 3(1):37–47, 2023. doi: 10.1785/0320220043.
- Cox, S. Injection-Driven Swarm Seismicity and Permeability Enhancement: Implications for the Dynamics of Hydrothermal Ore Systems in High Fluid-Flux, Overpressured Faulting Regimes—An Invited Paper. *Economic Geology*, 111(3):559–587, 2016. doi: 10.2113/econgeo.111.3.559.
- Dohrenwend, J. and Moring, B. Reconnaissance photogeologic map of young faults in the Vya 1°x2° quadrangle, Nevada–Oregon–California. *U.S. Geological Survey*, 1991. doi: 10.3133/mf2174.
- Faulds, J. and Henry, C. Tectonic influences on the spatial and temporal evolution of the Walker Lane: An incipient transform fault along the evolving Pacific–North American plate boundary. *Arizona Geological Society Digest*, 22:437–470, 2008.
- Faulds, J., Henry, C., and Hinz, N. Kinematics of the northern Walker Lane: An incipient transform fault along the Pacific–North American plate boundary. *Geology*, 33(6):505–508, 2005. doi: 10.1130/G21274.1.
- Gephart, J. and Forsyth, D. An improved method for determining the regional stress tensor using earthquake focal mechanism data: Application to the San Fernando Earthquake Sequence. *Journal of Geophysical Research: Solid Earth*, 89(B11):9305–9320, 1984. doi: 10.1029/JB089iB11p09305.
- Gold, R., Briggs, R., Personius, S., Crone, A., Mahan, S., and Angster, S. Latest Quaternary paleoseismology and evidence of distributed dextral shear along the Mohawk Valley fault zone, northern Walker Lane, California. *Journal of Geophysical Research: Solid Earth*, 119(6):5014–5032, 2014. doi: 10.1002/2014JB010987.
- Gutenberg, B. and Richter, C. Frequency of earthquakes in California. *Bulletin of the Seismological Society of America*, 34(4):185–188, 1944.
- Hainzl, S. Indications for a successively triggered rupture growth underlying the 2000 earthquake swarm in Vogtland/NW Bohemia. *Journal of Geophysical Research*, 107(B12), 2002. doi: 10.1029/2002JB001865.
- Hainzl, S. Seismicity patterns of earthquake swarms due to fluid intrusion and stress triggering. *Geophysical Journal International*, 159(3):1090–1096, 2004. doi: 10.1111/j.1365-246X.2004.02463.x.
- Hanks, T.  $f_{max}$ . *Bulletin of the Seismological Society of America*, 72(6A):1867–1879, 1982.
- Hanks, T. and Boore, D. Moment-magnitude relations in theory and practice. *Journal of Geophysical Research: Solid Earth*, 89(B7):6229–6235, 1984. doi: 10.1029/JB089iB07p06229.
- Hardebeck, J. and Michael, A. Damped regional-scale stress inversions: Methodology and examples for southern California and the Coalinga aftershock sequence. *Journal of Geophysical Research: Solid Earth*, 111(B11), 2006. doi: 10.1029/2005JB004144.
- Hatch, R., Abercrombie, R., Ruhl, C., and Smith, K. Earthquake Interaction, Fault Structure, and Source Properties of a Small Sequence in 2017 near Truckee, California. *Bulletin of the Seismological Society of America*, 108(5A):2580–2593, 2018. doi: 10.1785/0120180089.
- Hatch-Ibarra, R., Abercrombie, R., Ruhl, C., Smith, K., Hammond, W., and Pierce, I. The 2016 Nine Mile Ranch Earthquakes: Hazard and Tectonic Implications of Orthogonal Conjugate Faulting in the Walker Lane. *Bulletin of the Seismological Society of America*, 112(3):1727–1741, 2022. doi: 10.1785/0120210149.
- Hauksson, E., Stock, J., Bilham, R., Boese, M., Chen, X., and Fielding, E. Report on the August 2012 Brawley Earthquake Swarm in Imperial Valley, Southern California. *Seismological Research Letters*, 84(2):177–189, 2013. doi: 10.1785/0220120169.
- Hauksson, E., Ross, Z., and Cochran, E. Slow-Growing and Extended-Duration Seismicity Swarms: Reactivating Joints or Foliations in the Cahuilla Valley Pluton, Central Peninsular Ranges, Southern California. *Journal of Geophysical Research: Solid Earth*, 124(4):3933–3949, 2019. doi: 10.1029/2019JB017494.
- Hauksson, E., Olson, B., Grant, A., Andrews, J., Chung, A., and Hough, S. The Normal-Faulting 2020  $M_w$  5.8 Lone Pine, Eastern California, Earthquake Sequence. *Seismological Research Letters*, 92(2A):679–698, 2020. doi: 10.1785/0220200324.
- Hearn, E. and Humphreys, E. Kinematics of the southern Walker Lane Belt and motion of the Sierra Nevada block, California. *Journal of Geophysical Research: Solid Earth*, 103(B11):27033–27049, 1998. doi: 10.1029/98JB01390.
- Henry, C., Castor, S., Starkel, W., Ellis, B., Wolff, J., and Laravie, J. Geology and evolution of the McDermitt caldera, northern Nevada and southeastern Oregon, western USA. *Geosphere*, 13(4):1066–1112, 2017. doi: 10.1130/GES01454.1.
- Hill, D. A model for earthquake swarms. *Journal of Geophysical Research (1896-1977)*, 82(8):1347–1352, 1977. doi: 10.1029/JB082i008p01347.
- Hoffman, M. and Gelman, A. The No-U-Turn Sampler: Adaptively Setting Path Lengths in Hamiltonian Monte Carlo, 2011. ArXiv:1111.4246 [Cs, Stat].
- Holtkamp, S. and Brudzinski, M. Earthquake swarms in circum-Pacific subduction zones. *Earth and Planetary Science Letters*, 305(1):215–225, 2011. doi: 10.1016/j.epsl.2011.03.004.
- Hough, S. Observational constraints on earthquake source scaling: understanding the limits in resolution. *Tectonophysics*, 261(1):83–95, 1996. doi: 10.1016/0040-1951(96)00058-3.
- Hough, S. Empirical Green’s function analysis: Taking the next step. *Journal of Geophysical Research: Solid Earth*, 102(B3):5369–5384, 1997. doi: 10.1029/96JB03488.
- Ibs-von Seht, M., Plenefisch, T., and Klinge, K. Earthquake swarms in continental rifts — A comparison of selected cases in America, Africa and Europe. *Tectonophysics*, 452(1):66–77, 2008. doi: 10.1016/j.tecto.2008.02.008.
- Ichinose, G., Smith, K., and Anderson, J. Moment tensor solutions of the 1994 to 1996 Double Spring Flat, Nevada, earthquake sequence and implications for local tectonic models. *Bulletin of the Seismological Society of America*, 88(6):1363–1378, 1998.
- Kaneko, Y. and Shearer, P. Seismic source spectra and estimated stress drop derived from cohesive-zone models of circular subshear rupture. *Geophysical Journal International*, 197(2):1002–1015, 2014. doi: 10.1093/gji/ggu030.
- Kariche, J. The 2020 Monte Cristo (Nevada) Earthquake Sequence: Stress Transfer in the Context of Conjugate Strike-Slip Faults. *Tectonics*, 41(3):2020 006506, 2022. doi: 10.1029/2020TC006506.
- Koehler, R. Active faulting in the North Valleys region of

- Reno, Nevada: A distributed zone within the northern Walker Lane. *Geomorphology*, 326:38–53, 2019. doi: 10.1016/j.geomorph.2018.09.015.
- Koper, K., Pankow, K., Pechmann, J., Hale, J., Burlacu, R., and Yeck, W. Afterslip Enhanced Aftershock Activity During the 2017 Earthquake Sequence Near Sulphur Peak, Idaho. *Geophysical Research Letters*, 45(11):5352–5361, 2018. doi: 10.1029/2018GL078196.
- Kostrov, V. Seismic moment and energy of earthquakes, and the seismic flow of rock. *Izv. Acad. Sci. USSR. Phys. Solid Earth*, 1: 23–44, 1974.
- Krischer, L. *Mtspec Python Wrappers 0.3.2*. Zenodo, 2016. doi: 10.5281/zenodo.321789.
- Lerch, D., Klemperer, S., Egger, A., Colgan, J., and Miller, E. The northwestern margin of the Basin-and-Range Province, part 1: Reflection profiling of the moderate-angle (30°) Surprise Valley Fault. *Tectonophysics*, 488(1–4):143–149, 2010. doi: 10.1016/j.tecto.2009.05.028.
- Li, B., Smith, J., and Ross, Z. Basal nucleation and the prevalence of ascending swarms in Long Valley caldera. *Science Advances*, 7(35):8368, 2021. doi: 10.1126/sciadv.abi8368.
- Lohman, R. and McGuire, J. Earthquake swarms driven by aseismic creep in the Salton Trough, California. *Journal of Geophysical Research*, 112(B4), 2007. doi: 10.1029/2006JB004596.
- Lomax, A., Virieux, J., Volant, P., and Berge-Thierry, C. Probabilistic Earthquake Location in 3D and Layered Models. In Thurber, C. and Rabinowitz, N., editors, *Advances in Seismic Event Location*, page 101–134. Springer Netherlands, Dordrecht, 2000. doi: 10.1007/978-94-015-9536-0\_5.
- Lomax, A., Zollo, A., Capuano, P., and Virieux, J. Precise, absolute earthquake location under Somma–Vesuvius volcano using a new three-dimensional velocity model. *Geophysical Journal International*, 146(2):313–331, 2001. doi: 10.1046/j.0956-540x.2001.01444.x.
- Madariaga, R. Dynamics of an expanding circular fault. *Bulletin of the Seismological Society of America*, 66(3):639–666, 1976.
- Mesimeri, M., Pankow, K., Baker, B., and Hale, J. Episodic Earthquake Swarms in the Mineral Mountains, Utah Driven by the Roosevelt Hydrothermal System. *Journal of Geophysical Research: Solid Earth*, 126(6):2021 021659, 2021. doi: 10.1029/2021JB021659.
- Michael, A. J. Determination of stress from slip data: Faults and folds. *Journal of Geophysical Research: Solid Earth*, 89(B13): 11517–11526, 1984. doi: 10.1029/JB089iB13p11517.
- Michael, A. J. Use of focal mechanisms to determine stress: A control study. *Journal of Geophysical Research: Solid Earth*, 92(B1): 357–368, 1987. doi: 10.1029/JB092iB01p00357.
- Mogi, K. Experimental study on the mechanism of the earthquake occurrences of volcanic origin. *Bulletin of Volcanology*, 26(1): 197–208, 1963. doi: 10.1007/BF02597286.
- Mousavi, S., Sheng, Y., Zhu, W., and Beroza, G. STanford Earthquake Dataset (STEAD): A Global Data Set of Seismic Signals for AI. *IEEE Access*, 7:179464–179476, 2019. doi: 10.1109/ACCESS.2019.2947848.
- Mousavi, S., Ellsworth, W., Zhu, W., Chuang, L., and Beroza, G. Earthquake transformer—an attentive deep-learning model for simultaneous earthquake detection and phase picking. *Nature Communications*, 11(1):3952, 2020. doi: 10.1038/s41467-020-17591-w.
- Munafò, I., Malagnini, L., and Chiaraluca, L. On the Relationship between  $M_w$  and  $M_L$  for Small Earthquakes. *Bulletin of the Seismological Society of America*, 106(5):2402–2408, 2016. doi: 10.1785/0120160130.
- Omori, F. Investigation of aftershocks. *Rep. Earthquake Inv. Comm*, 2:103–139, 1894.
- Owens, T., Crotwell, H., Groves, C., and Oliver-Paul, P. SOD: Standing Order for Data. *Seismological Research Letters*, 75(4): 515–520, 2004. doi: 10.1785/gssrl.75.4.515-a.
- Personius, S., Briggs, R., Maharrey, J., Angster, S., and Mahan, S. A paleoseismic transect across the northwestern Basin and Range Province, northwestern Nevada and northeastern California, USA. *Geosphere*, 13(3):782–810, 2017. doi: 10.1130/GES01380.1.
- Pierce, K. and Morgan, L. Chapter 1: The track of the Yellowstone hot spot: Volcanism, faulting, and uplift. In Link, P., Kuntz, M., and Piatt, L., editors, *Regional Geology of Eastern Idaho and Western Wyoming*, volume 179, page 0. Geological Society of America, 1992. doi: 10.1130/MEM179-p1.
- Pollitz, F., Wicks, C., and Hammond, W. Kinematic Slip Model of the 2021 M 6.0 Antelope Valley, California, Earthquake. *The Seismic Record*, 2(1):20–28, 2022. doi: 10.1785/0320210043.
- Prieto, G., Parker, R., and Vernon III, F. A Fortran 90 library for multitaper spectrum analysis. *Computers & Geosciences*, 35(8): 1701–1710, 2009. doi: 10.1016/j.cageo.2008.06.007.
- Richter, C. An instrumental earthquake magnitude scale. *Bulletin of the Seismological Society of America*, 25(1):1–32, 1935.
- Ross, Z. and Cochran, E. Evidence for Latent Crustal Fluid Injection Transients in Southern California From Long-Duration Earthquake Swarms. *Geophysical Research Letters*, 48(12):2021 092465, 2021. doi: 10.1029/2021GL092465.
- Ross, Z., Rollins, C., Cochran, E., Hauksson, E., Avouac, J.-P., and Ben-Zion, Y. Aftershocks driven by afterslip and fluid pressure sweeping through a fault-fracture mesh. *Geophysical Research Letters*, 44(16):2017 074634, 2017. doi: 10.1002/2017GL074634.
- Ross, Z., Idini, B., Jia, Z., Stephenson, O., Zhong, M., and Wang, X. Hierarchical interlocked orthogonal faulting in the 2019 Ridgecrest earthquake sequence. *Science*, 366(6463):346–351, 2019. doi: 10.1126/science.aaz0109.
- Ross, Z., Cochran, E., Trugman, D., and Smith, J. 3D fault architecture controls the dynamism of earthquake swarms. *Science*, 368(6497):1357–1361, 2020. doi: 10.1126/science.abb0779.
- Ruhl, C., Abercrombie, R., Smith, K., and Zaliapin, I. Complex spatiotemporal evolution of the 2008  $M_w$  4.9 Mogul earthquake swarm (Reno, Nevada): Interplay of fluid and faulting. *Journal of Geophysical Research: Solid Earth*, 2016a. doi: 10.1002/2016JB013399.
- Ruhl, C., Smith, K., Kent, G., and Seaman, T. Seismotectonic and Seismic Hazard Implications for the Reno-Tahoe Area of the Walker Lane in Nevada and California. *Applied Geology of California*, 2016b.
- Ruhl, C., Abercrombie, R., and Smith, K. Spatiotemporal Variation of Stress Drop During the 2008 Mogul, Nevada, Earthquake Swarm. *Journal of Geophysical Research: Solid Earth*, 122(10): 2017 014601, 2017. doi: 10.1002/2017JB014601.
- Ruhl, C., Morton, E., Bormann, J., Hatch-Ibarra, R., Ichinose, G., and Smith, K. Complex Fault Geometry of the 2020  $M_{ww}$  6.5 Monte Cristo Range, Nevada, Earthquake Sequence. *Seismological Research Letters*, 92(3):1876–1890, 2021. doi: 10.1785/0220200345.
- Sadeghi Chorsi, T., Braunmiller, J., Deng, F., and Dixon, T. Afterslip From the 2020 M 6.5 Monte Cristo Range, Nevada Earthquake. *Geophysical Research Letters*, 49(17):2022 099952, 2022. doi: 10.1029/2022GL099952.
- Salvatier, J., Wiecki, T., and Fonnesbeck, C. Probabilistic programming in Python using PyMC3. *PeerJ Computer Science*, 2:55, 2016. doi: 10.7717/peerj-cs.55.
- Sato, T. and Hirasawa, T. Body Wave Spectra from Propagating

- Shear Cracks. *Journal of Physics of the Earth*, 21(4):415–431, 1973. doi: 10.4294/jpe1952.21.415.
- Schaff, S. The 1968 Adel, 1976. Retrieved from.
- Scholz, C. The frequency-magnitude relation of microfracturing in rock and its relation to earthquakes. *Bulletin of the Seismological Society of America*, 58(1):399–415, 1968.
- Scholz, C. H. On the stress dependence of the earthquake b value. *Geophysical Research Letters*, 42(5):1399–1402, 2015. doi: 10.1002/2014GL062863.
- Sethanant, I., Nissen, E., Pousse-Beltran, L., Bergman, E., and Pierce, I. The 2020  $M_w$  6.5 Monte Cristo Range, Nevada, Earthquake: Anatomy of a Crossing-Fault Rupture through a Region of Highly Distributed Deformation. *Bulletin of the Seismological Society of America*, 113(3):948–975, 2023. doi: 10.1785/0120220166.
- Shapiro, S., Huenges, E., and Borm, G. Estimating the crust permeability from fluid-injection-induced seismic emission at the KTB site. *Geophysical Journal International*, 131(2):15–18, 1997. doi: 10.1111/j.1365-246X.1997.tb01215.x.
- Shearer, P., Abercrombie, R., Trugman, D., and Wang, W. Comparing EGF Methods for Estimating Corner Frequency and Stress Drop From P Wave Spectra. *Journal of Geophysical Research: Solid Earth*, 124(4):3966–3986, 2019. doi: 10.1029/2018JB016957.
- Shearer, P., Abercrombie, R., and Trugman, D. Improved Stress Drop Estimates for  $M$  1.5 to 4 Earthquakes in Southern California From 1996 to 2019. *Journal of Geophysical Research: Solid Earth*, 127(7):2022 024243, 2022. doi: 10.1029/2022JB024243.
- Shelly, D. and Hardebeck, J. Illuminating Faulting Complexity of the 2017 Yellowstone Maple Creek Earthquake Swarm. *Geophysical Research Letters*, 46(5):2544–2552, 2019. doi: 10.1029/2018GL081607.
- Shelly, D., Ellsworth, W., and Hill, D. Fluid-faulting evolution in high definition: Connecting fault structure and frequency-magnitude variations during the 2014 Long Valley Caldera, California, earthquake swarm. *Journal of Geophysical Research: Solid Earth*, 121(3):1776–1795, 2016. doi: 10.1002/2015JB012719.
- Shelly, D., Skoumal, R., and Hardebeck, J. Fracture-Mesh Faulting in the Swarm-Like 2020 Maacama Sequence Revealed by High-Precision Earthquake Detection, Location, and Focal Mechanisms. *Geophysical Research Letters*, 50(1):2022 101233, 2023. doi: 10.1029/2022GL101233.
- Sibson, R. Earthquake rupturing as a mineralizing agent in hydrothermal systems. *Geology*, 15(8):701–704, 1987. doi: 10.1130/0091-7613(1987)15.
- Sibson, R. Structural permeability of fluid-driven fault-fracture meshes. *Journal of Structural Geology*, 18(8):1031–1042, 1996. doi: 10.1016/0191-8141(96)00032-6.
- Sykes, L. Earthquake swarms and sea-floor spreading. *Journal of Geophysical Research (1896-1977)*, 75(32):6598–6611, 1970. doi: 10.1029/JB075i032p06598.
- Trugman, D. Resolving Differences in the Rupture Properties of  $M_5$  Earthquakes in California Using Bayesian Source Spectral Analysis. *Journal of Geophysical Research: Solid Earth*, 127(4):2021 023526, 2022. doi: 10.1029/2021JB023526.
- Trugman, D. and Shearer, P. Application of an improved spectral decomposition method to examine earthquake source scaling in southern California. *Journal of Geophysical Research: Solid Earth*, 122(4):2017 013971, 2017a. doi: 10.1002/2017JB013971.
- Trugman, D. and Shearer, P. GrowClust: A Hierarchical Clustering Algorithm for Relative Earthquake Relocation, with Application to the Spanish Springs and Sheldon, Nevada, Earthquake Sequences. *Seismological Research Letters*, 88(2A):379–391, 2017b. doi: 10.1785/0220160188.
- Trugman, D., Ross, Z., and Johnson, P. Imaging Stress and Faulting Complexity Through Earthquake Waveform Similarity. *Geophysical Research Letters*, 47(1):2019 085888, 2020. doi: 10.1029/2019GL085888.
- Trugman, D., Chamberlain, C., Savvaidis, A., and Lomax, A. GrowClust3D.jl: A Julia Package for the Relative Relocation of Earthquake Hypocenters Using 3D Velocity Models. *Seismological Research Letters*, 94(1):443–456, 2022. doi: 10.1785/0220220193.
- Trugman, D., Brune, J., Smith, K., Louie, J., and Kent, G. The Rocks That Did Not Fall: A Multidisciplinary Analysis of Near-Source Ground Motions From an Active Normal Fault. *AGU Advances*, 4(2):2023 000885, 2023. doi: 10.1029/2023AV000885.
- Uhrhammer, R., Loper, S., and Romanowicz, B. Determination of local magnitude using BDSN broadband records. *Bulletin of the Seismological Society of America*, 86(5):1314–1330, 1996. doi: 10.1785/BSSA0860051314.
- van der Elst, N. B-Positive: A Robust Estimator of Aftershock Magnitude Distribution in Transiently Incomplete Catalogs. *Journal of Geophysical Research: Solid Earth*, 126(2):2020 021027, 2021. doi: 10.1029/2020JB021027.
- Vavryčuk, V. Iterative joint inversion for stress and fault orientations from focal mechanisms. *Geophysical Journal International*, 199(1):69–77, 2014. doi: 10.1093/gji/ggu224.
- Vidale, J. and Shearer, P. A survey of 71 earthquake bursts across southern California: Exploring the role of pore fluid pressure fluctuations and aseismic slip as drivers. *Journal of Geophysical Research*, 111(B5), 2006. doi: 10.1029/2005JB004034.
- von Seggern, D., Smith, K., and Preston, L. Seismic Spatial-Temporal Character and Effects of a Deep (25–30 km) Magma Intrusion below North Lake Tahoe, California–Nevada. *Bulletin of the Seismological Society of America*, 98(3):1508–1526, 2008. doi: 10.1785/0120060240.
- Wang, K., Dreger, D., Burgmann, R., and Taira, T. Finite-Source Model of the. *Seismological Research Letters*, 94(3):1352–1366, 2023. doi: 10.1785/0220220262.
- Wesnousky, S. Active faulting in the Walker Lane. *Tectonics*, 24(3), 2005. doi: 10.1029/2004TC001645.
- Wessel, P., Luis, J., Uieda, L., Scharroo, R., Wobbe, F., Smith, W., and Tian, D. The Generic Mapping Tools Version 6. *Geochemistry, Geophysics, Geosystems*, 20(11):5556–5564, 2019. doi: 10.1029/2019GC008515.
- Woollam, J., Münchmeyer, J., Tilmann, F., Rietbrock, A., Lange, D., and Bornstein, T. SeisBench—A Toolbox for Machine Learning in Seismology. *Seismological Research Letters*, 93(3):1695–1709, 2022. doi: 10.1785/0220210324.
- Zheng, A., Chen, X., and Xu, W. Present-Day Deformation Mechanism of the Northeastern Mina Deflection Revealed by the 2020  $M_w$  6.5 Monte Cristo Range Earthquake. *Geophysical Research Letters*, 47(22):2020 090142, 2020. doi: 10.1029/2020GL090142.

The article *Unraveling the Evolution of an Unusually Active Earthquake Sequence Near Sheldon, Nevada* © 2023 by D. T. Trugman is licensed under CC BY 4.0.